Korean J. Chem. Eng., 36(6), 1004-1012 (2019)
DOI: 10.1007/s11814-019-0282-2

pISSN: 0256-1115
eISSN: 1975-7220

Effect of filler size on thermal properties of paraffin/silver nanoparticle composites

In-Hyun Kim, Hyo-Won Sim, Hee-Hyeon Hong, Dong-Woo Kim, Wonjoo Lee, and Dong-Koo Lee†

Advanced Industrial Chemistry Research Center, Korea Research Institute of Chemical Technology, Ulsan 44412, Korea
(*Received 17 February 2019 • accepted 23 April 2019*)

Abstract−The effects of different filler sizes on the thermal properties were investigated in a thermal conductive composite (TCC) phase-change material (PCM) with three sizes (9, 65, and 300 nm) of silver nanoparticles (Ag NPs). Ag NP/paraffin composites (Ag/PW) were prepared by dispersing 0.5, 1.0, 1.5, and 2.0 wt% of Ag NPs stably into molten paraffin using ultra-sonication and then solidifying the mixture. The thermal properties of the composite, such as the thermal conductivity, latent heat capacity, and thermal stability, were characterized by laser flash analysis (LFA), differential scanning calorimetry (DSC), and thermal gravimetric analysis (TGA), respectively. The degree and trend of the enhancement of the thermal properties differed based on the Ag NP size, and the efficiency increased with a decreasing particle size. In addition, we adopted some theoretical models to describe the behavior of thermal conductivity enhancement in this study. The results were explained by the difference in the interfacial area and degree of construct cluster of the Ag NPs, which were dependent on the particle size.

Keywords: Phase Change Material (PCM), Silver Nanoparticle (Ag NPs), Filler Size Effect, Thermal Conductivity, Latent Heat Capacity

INTRODUCTION

Thermal energy management, such as thermal energy storage (TES), is considered one of the most prospective technologies for renewable energy utilization and precision electronic devices [1-4]. For decades, phase change materials (PCMs) have been attractive for the efficient and economical storage of thermal energy by a phase change process. Among the various PCMs, paraffins are mainly used owing to their large latent heat capacity, physical/chemical stability, and extremely small volume change during the phase change process [5]. However, the low thermal conductivity of paraffins restricts their commercial applications.

To overcome these drawbacks, various studies have been developed for a thermally conductive composite (TCC), which is a mixture of high-thermally conductive fillers and a PCM. Generally, carbon-, metal/metal-oxide, and ceramics, such as boron nitride (BN), aluminum nitride (AlN), and silica carbide (SiC), are widely used as thermally conductive fillers owing to the high-thermal conductivity and chemical stability at low and high temperatures. For example, nickel (Ni)/epoxy [6], silver (Ag)/epoxy [7], copper (Cu)/paraffin [8], CuO/eicosane [9], carbon nanoplatelets/paraffin [10], multi-walled carbon nanotube (MWCNT)/paraffin [11], and graphene/paraffin [12] composites have been used to improve the thermal conductivity of paraffin PCM.

The thermal conductivity of a TCC is affected by the various physical/chemical properties of the filler [13-16], especially the filler size. Generally, when the filler size is micro-scale, large-sized fillers exhibit a high thermal conductivity because of the small interfacial area that reduces phonon scattering and the thermal energy transfer to the surroundings [17-19]. However, there are controversial reports on the effect of the filler size. Pashayi et al. reported that the addition of nanoparticles as fillers creates a higher thermal conductivity than that with microparticles. They showed that the Ag/epoxy nanocomposite exhibited approximately a 50 times greater thermal conductivity than that of the microcomposite under the same condition [20]. The nanoparticles showed a larger thermal conductivity enhancement when they formed a thermally conductive network in the composite; however, the microparticles did not show this trend.

In addition, filler often provides other positive effects to the thermal/mechanical properties of the TCC, such as the modulus, strength, and thermal stability [21,22]. However, the addition of the filler does not always show a positive effect. Numerous studies have reported that the latent heat capacity of the TCC decreases with an increase of the amount of filler, which leads to performance degradation of the PCM [23,24]. The reduction of the latent heat capacity is a critical problem because it is the most important factor in TES. Therefore, improving the thermal conductivity while minimizing the latent heat capacity reduction of the TCC is an important goal in thermal energy management technology.

Stable silver nanoparticle (Ag NP)/paraffin composites (Ag/PW) were prepared in a low mass fraction range (0.5, 1.0, 1.5, and 2.0 wt%) to determine the filler size effect on the thermal properties. Three sizes of Ag NPs (9, 65, and 300 nm, respectively) were synthesized and used as a thermal conductive filler. Ag NP is a suitable filler because it is a high thermally conductive material (~400 W/m·K) and has a high density (~10.49 g/ml at room temperature). Ag NPs can be synthesized by a convenient solvothermal method with oleylamine (OAm), which can be used as a reductant and surface stabilizer and can improve the dispersibility of the Ag NPs in the molten paraffin. OAm capped Ag NPs and molten paraffin were homogeneously mixed through ultra-sonicate dispersion to obtain

†To whom correspondence should be addressed.
E-mail: dklee@krict.re.kr, dklee6677@gmail.com

Ag/PWs. This study investigated the particles size effect on the thermal properties of the composite, such as the thermal conductivity, stability, and heat capacity, under the same condition.

EXPERIMENTAL METHOD

1. Materials

Silver nitrate ($AgNO_3$), silver oxide (Ag_2O), silver acetate (CH_3COOAg), oleylamine (OAm), and paraffin were purchased from Sigma-Aldrich, USA. Methanol, n-hexane, and toluene were purchased from DEAJUNG Chemical & Materials Co., Ltd., S. Korea. All chemicals were used without any further purification or treatment.

2. OAm-capped Ag NP Synthesis

The Ag NPs were synthesized via a modified Osterloh method [25]. The size of the Ag NPs was controlled by the type of precursor. As a typical synthesis process, 2.0-2.5 g of silver precursor was dissolved in OAm and mixed with toluene in a 3-neck round-bottom flask with a condenser. The mixture was heated at 120 °C, and the reflux system was maintained for overnight with vigorous magnet stirring in air. The color of the mixture solution gradually changed from colorless to yellow and deep-dark brown, sequentially, indicating the formation of the Ag NPs. The detailed synthesis conditions are summarized in Table 1.

After completion of the reaction, the solution was cooled to room temperature and products were precipitated by addition of 100 ml methanol. The precipitates were collected and dissolved in 10 ml of n-hexane after discarding the supernatant, and the dissolved mixture was precipitated again with 50 ml of methanol. After three repetitions of this purification process, the final product was dried in vacuum oven.

3. Ag/PW Preparation

0.5, 1.0, 1.5, and 2.0 wt% Ag/PW prepared by OAm-capped Ag NPs were added to molten paraffin. Each 10 g of Ag/PW were used for sampling and analysis. For example, a 0.5 wt% sample was prepared by the following procedure: 9.95 g of paraffin was melted at 80 °C in 100 ml beaker, and 0.05 g of OAm-capped Ag NPs was dispersed in the molten paraffin with bar type ultrasonication instrument at 20 kHz for 2 h. After dispersion process, the molten Ag/PW mixture was poured into a pre-heated brass mold and degassed in a vacuum oven for 30 min at 80 °C. The degassed Ag/PW composite was then cooled to room temperature using cold water and removed from the brass mold. The same procedure was repeated for the 1 (0.1 g), 1.5 (0.15 g) and 2 (0.2 g) wt% of Ag/PW samples.

4. Characterization

The size and shape of the Ag NPs and the Ag/PW morphologies were investigated by field-emission scanning electron microscopy (FE-SEM) (TESAN, MIRA 3) and high-resolution transmittance electron microscopy (JEOL, JEM-2100F) with an accelerating voltage of 15 kV and 200 kV to collect Ag NPs images. FE-SEM and HR-TEM samples for Ag NPs were prepared by dropcasting the colloidal dispersion in n-hexane onto a clean silicon wafer and an amorphous carbon-coated copper grid, respectively. The morphology of Ag/PW was observed with FE-SEM, and all samples were coated with platinum before analysis. The crystal structure of the Ag NPs and Ag/PW was investigated using x-ray diffractometer (XRD, Rigaku, Ultima IV) employing Cu kα radiation (λ=1.5406 Å). Scanning angles were 3-90° with scanning mode at the rate of 5°/min. Fourier transform infrared spectroscopy (FT-IR) (Thermo Fisher Scientific Nicolet Continuum IR Microscope) was used to analyze the chemical composition of the Ag NPs and Ag/PW. A zinc selenide (ZnSe) crystal attachment together with a mercury cadmium telluride (MCT) and deuterated triglycine sulfate (DTS) detector was used to record the attenuated total reflection (ATR). The latent heat capacity of samples was analyzed by differential scanning calorimeter (DSC) (TA instrument DSC Q2000) with accuracy of ±0.2 °C. 10 mg of sample were placed on an aluminum pan, and tested from 25 °C to 90 °C with heating increment of 10 °C/min. The thermal degradation was tested by a thermal gravimetric analyzer (TGA) (TA instrument TGA Q500). Each sample was weighted 10 mg and placed on a ceramic pan. The range of test temperature was controlled from 25 to 700 °C with heating increment of 10 °C/min. During DSC and TGA experiments, nitrogen gas was purged at a rate of 20 mL/min. The thermal conductivities of the paraffin and Ag/PW were determined with a laser-flash analyzer (Netzsch Instrument, LFA647) at 25 °C.

RESULTS AND DISCUSSION

The overall synthesis of the Ag NPs and Ag/PW is shown in Fig. 1. Three sizes of Ag NPs were synthesized by reducing different Ag precursors using OAm as the reducing and capping agent. The morphology and size of the synthesized Ag NPs were observed by transmission electron microscopy (TEM) and SEM, as shown in Fig. 2. The electron microscopy images revealed that the average sizes of the Ag NPs were 9±1.0 nm (Fig. 2(a), $AgNO_3$), 65±14 nm (Fig. 2(b), Ag_2O), and 300±60 nm (Fig. 2(c), CH_3COOAg).

The crystallinity of the Ag NPs was confirmed by XRD analysis. Fig. 3(a) shows the XRD patterns of the synthesized Ag NPs, containing four strong peaks at the 2θ values of 38.08°, 44.26°, 64.4°, and 77.36°, corresponding to the (111), (200), (220), and (311) lattice planes of the face-centered cubic structure of pure Ag (JCPDS no. 19-0629). Based on the most intense (111) peak of the XRD data, the crystallite size of the Ag NPs could be determined by applying the Scherrer equation [26]. The crystallite sizes of the Ag NPs were calculated to be 8.9, 58, and 150 nm for the nanoparticles synthesized with $AgNO_3$, Ag_2O, and CH_3COOAg precursors, respectively. These values agreed well with the SEM and TEM measure-

Table 1. Synthesis conditions for the preparation of silver nanoparticles

Precursor type	Precursor (g)	Oleylamine (ml)	Toluene (ml)	Temperature (°C)	Time (h)	Mean size (nm)
$AgNO_3$	2.5	20	50	120	12	9±1.0
Ag_2O	2.0	15	100	120	16	65±14
CH_3COOAg	2.5	10	50	120	16	300±60

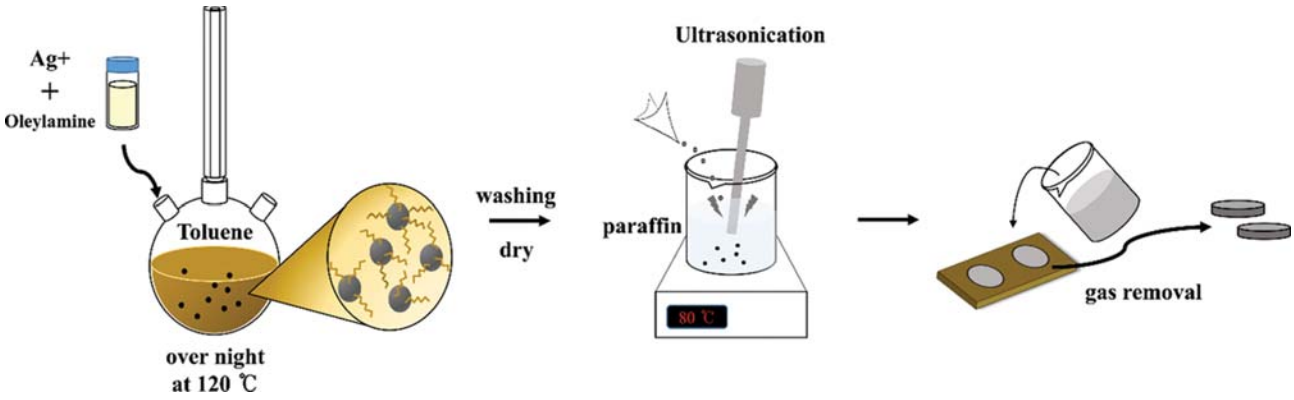

Fig. 1. Schematic illustration of the Ag NP synthesis with OAm in toluene and the preparation of Ag/PW.

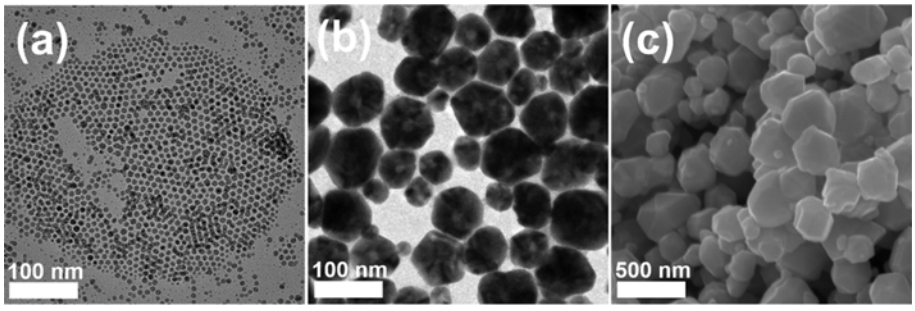

Fig. 2. Electron microscopy images of the Ag NPs synthesized by different silver precursors. The average sizes of each Ag NP are (a) 9-nm, (b) 65-nm, and (c) 300-nm, respectively. See Table 1 for detailed synthesis conditions.

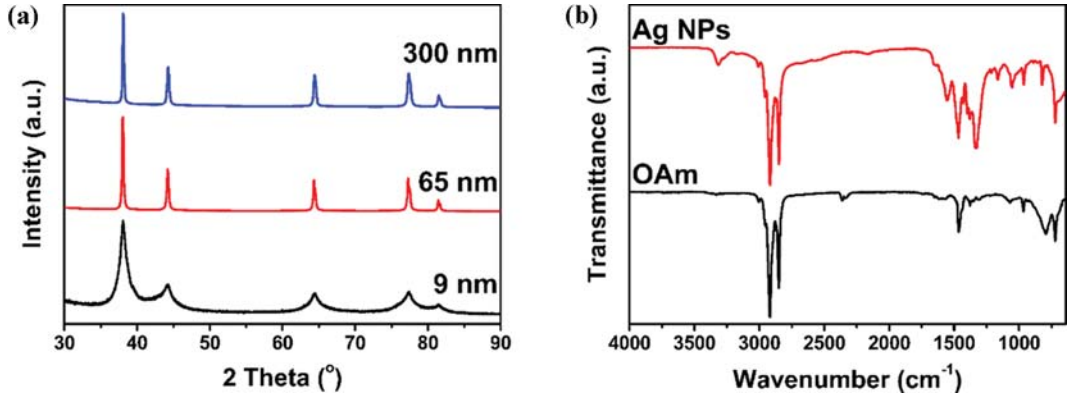

Fig. 3. (a) XRD patterns and (b) FTIR spectra of the Ag NPs with OAm.

ments, except for the 300-nm particle. Fig. 3(b) shows the FT-IR spectra of the OAm and synthesized Ag NPs. The Ag NP surface was covered with OAm, as confirmed by the FT-IR spectra of the two samples. The peaks at 2,850 and 2,919 cm^{-1} were related to the symmetric and asymmetric CH_2 stretching vibration, respectively, and the peaks at 1,460 and 3,004 cm^{-1} were assigned to the CH_2 bending and C-H stretching vibrations, respectively. The characteristic band of the Ag NPs was associated with weak N-H bending at 1,650 cm^{-1} and N-H stretching at 3,300 cm^{-1} [27-29]. Based on the FT-IR spectra, the OAm was adsorbed on the Ag NP surface.

The Ag NPs were mixed with molten paraffin via ultra-sonication. The Ag NPs were capped with OAm, which improved the stable dispersion in the molten paraffin owing to the long-carbon chains in the molecular structure of OAm. The surface morphology of the Ag/PW was characterized by FE-SEM. Fig. 4(a) to (c) shows the surface of the paraffin with 9-, 65-, and 300-nm Ag/PW at 0.5 wt% of Ag NPs, respectively. No particles were visible on the surface, except for the 300-nm Ag/PW, indicating that the Ag NPs were well-dispersed without aggregation at 0.5 wt%. However, small dots on the Ag/PW surface were observed, which represented a cluster formed by the aggregation of the Ag NPs at 1.0 wt%, as shown in Fig. 4(d) to (f). With the increase of the Ag NP concentration, each particle could aggregate, and the number of clusters varied depending on the particle size. The cluster formation by aggrega-

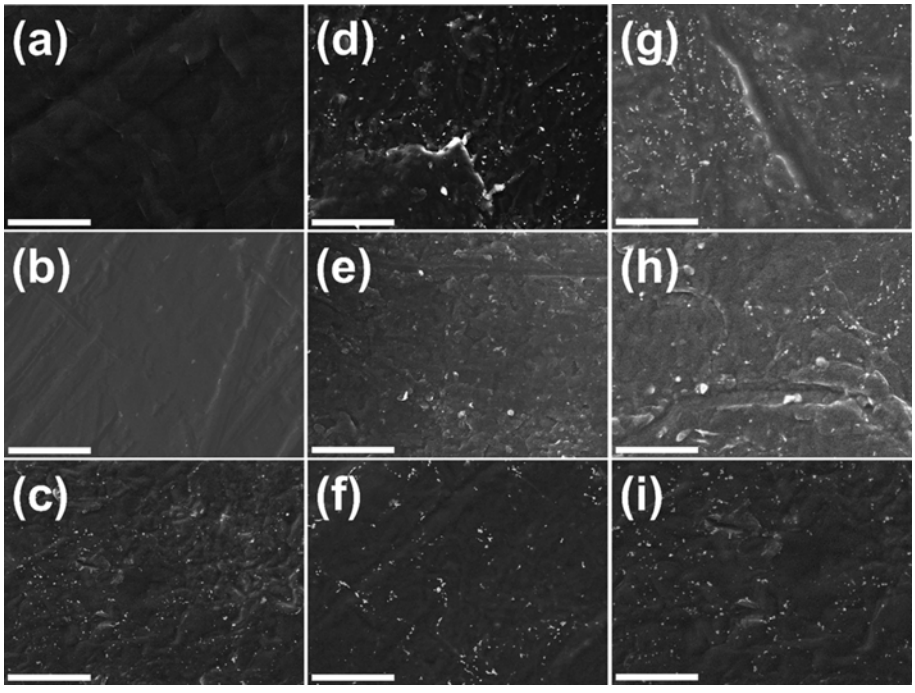

Fig. 4. FE-SEM images of (a) 9-nm, (b) 65-nm, and (c) 300-nm Ag/PW at 0.5 wt%, (d) 9-nm, (e) 65-nm, and (f) 300-nm Ag/PW at 1.0 wt%, and (g) 9-nm, (h) 65-nm, (i) 300-nm Ag/PW at 2.0 wt% (scale bar: 50 μm).

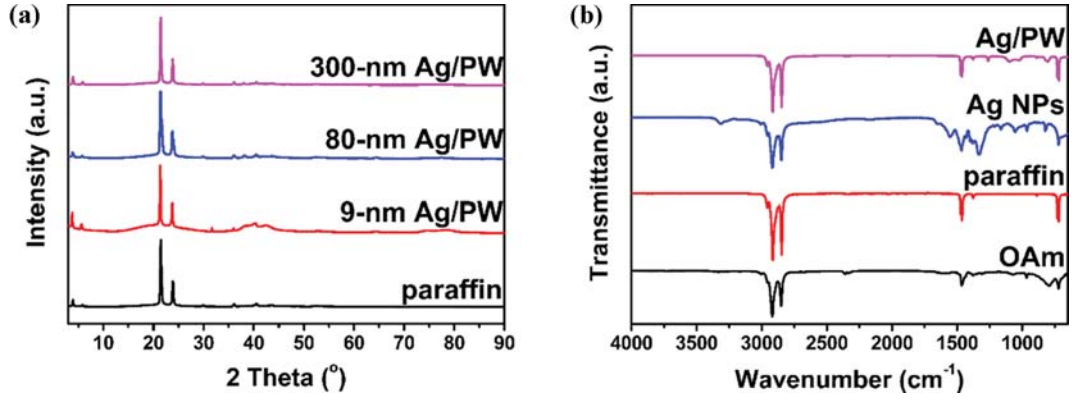

Fig. 5. (a) XRD patterns of the pure paraffin and Ag/PW with different Ag NP sizes at 2.0 wt%. Image (b) shows the FTIR spectra of the paraffin and Ag/PW.

tion was more active for the 9-nm Ag/PW (Fig. 4(d)) than those for the 65- and 300-nm Ag/PW (Fig. 4(e) and (f)) because the small particles have a higher surface energy than that of the large particles. In addition, although the amount of Ag NPs increased to 2.0 wt% (Fig. 4(d), (h), and (i)), no significant change was observed compared to 1.0 wt% of Ag NPs.

The crystallinity and chemical interaction between the Ag NPs and paraffin were determined using XRD and an FTIR analysis. Fig. 5 shows the XRD patterns of the paraffin, Ag NPs, and Ag/PWs. In Fig. 5(a), the sharp strong peaks at approximately 21° and 23° indicated the [110] and [200] non-crystalline structures of paraffin for all samples (JCPDS no. 40-1995). Weak peaks were observed at approximately 38° and 44°, corresponding to the Ag NPs, as shown in Fig. 3(a). The XRD peak of Ag/PW was not different from that of paraffin; therefore, the crystal structure of the paraffin was maintained without any critical change. Fig. 5(b) shows the FT-IR spectra of the Ag NPs, paraffin, and Ag/PW. The FT-IR spectra indicated that there were no significant changes in the FT-IR peak of the Ag/PW, compared to that of the paraffin. Peaks observed at 2,850 and 2,919 cm^{-1}, related to the symmetric and asymmetric CH_2 stretching, at 1,460 and 3,004 cm^{-1} were assigned to CH_2-bending and the C-H-stretching vibration, respectively. The peak at 718 cm^{-1} for CH_2 and CH_3 rocking mode, derived from the long carbon chains of the paraffin and OAm. All major peaks for the samples were observed, except for the small peak shifts, indicating that there was physical adsorption between the paraffin and Ag NPs without chemical interactions.

The thermal stability of the Ag/PW was analyzed using TGA,

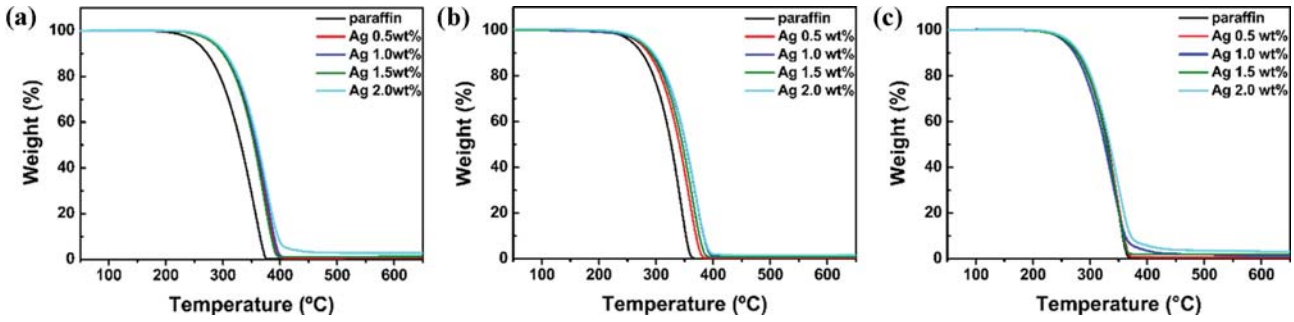

Fig. 6. Measurement of the thermal stability using TGA: (a) 9-nm, (b) 65-nm and (c) 300-nm Ag/PW.

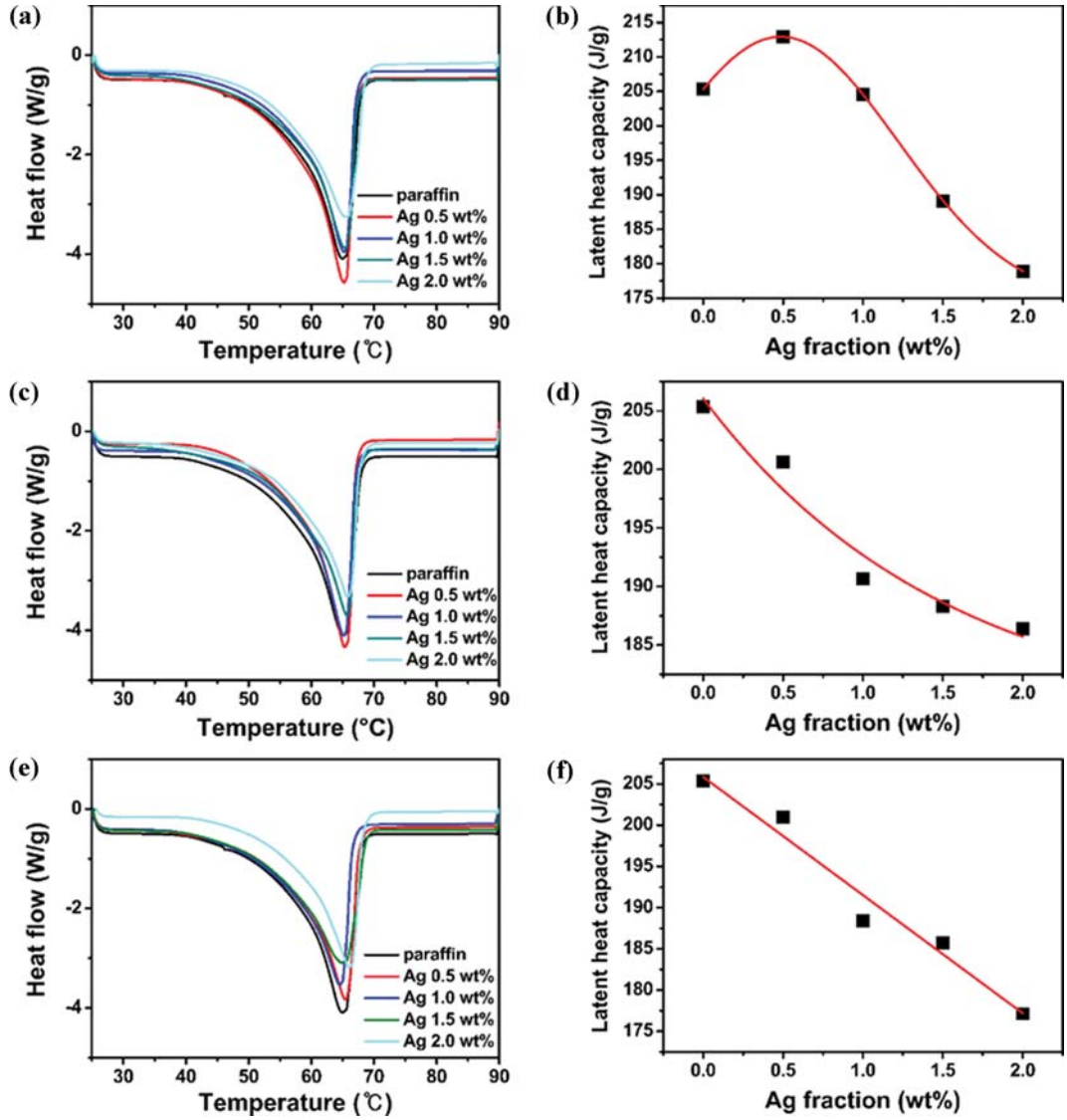

Fig. 7. The latent heat capacity of the paraffin and Ag/PWs: (a) and (d) 9-nm, (b) and (e) 65-nm, and (c) and (f) 300-nm Ag NPs.

as shown in Fig. 6. Compared to paraffin, the decomposition temperature of Ag/PW increased approximately 5-50 °C depending on the Ag NP sizes. This result indicated that the thermal stability of the Ag/PW was improved by the addition of the Ag NPs. The thermal conductivity enhancement trend was different based on the Ag NP size. The 9-nm Ag/PW showed a high thermal stability improvement even at 0.5 wt%, and the 65-nm Ag/PW exhibited a thermal stability increase as the particle content increased. However, the thermal stability of the 300-nm Ag/PW did not differ from the paraffin and slightly increased. This can be explained by the inter-

action between the paraffin and Ag NPs. Xiang et al. [30] and Lin et al. [31] reported that the thermal stability of Cu/PW was improved by the physical bonding interaction between the paraffin and Cu nanostructures, and thus, the heat-resistance improved. Because the 9-nm Ag NPs have a larger surface area than the 65- and 300-nm Ag NPs under the same condition, allowing an increased interaction with the surrounding paraffin causes a thermal stability improvement of Ag/PW.

Fig. 7(a)-(c) shows the DSC curves of the paraffin and Ag/PW. There was only one peak between 40 and 70 °C, which was attributed to the solid-liquid phase change processes for the paraffin and Ag/PW. This result is consistent with the XRD analyses. The main structure of paraffin did not change when the Ag NPs were added [32]. From Fig. 7(d)-(f), the latent heat capacity of paraffin was 202 J/g, while Ag/PW decreased as the content of the particles increased; however, the latent heat capacity slightly increased to 213 J/g when 0.5 wt% of 9-nm Ag NPs were loaded. The increase in the latent heat capacity by the filler can be explained by the heterogeneous nucleation during the solidification step. Tang et al. reported that the latent heat capacity of a paraffin composite with 1.0 and 5.0 wt% functionalized-multiwall carbon nanotubes (f-MWCNTs) increased because the f-MWCNTs function as a heterogeneous nucleation agent, which is advantageous for the crystallization growth of paraffin [33]. In addition, a larger surface area allows an easy interaction with the paraffin, improving the Ag/PW crystallization. However, for a further increase of the 9-nm Ag NPs to 1.0 wt%, the latent heat capacity of the Ag/PW decreased to 200 J/g owing to the reduced ratio of the phase change component paraffin in the composite. This result indicated that, in order to maintain the heat capacity, the filler size was an important factor as well as the filler content.

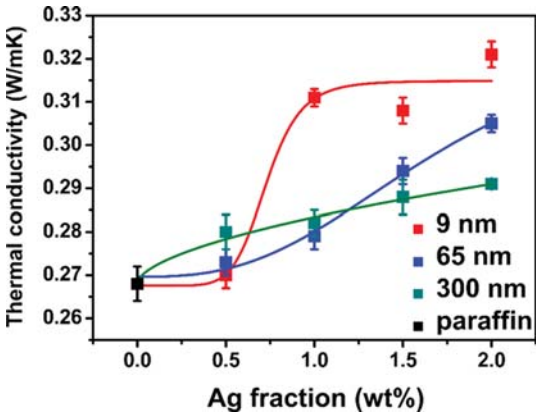

Fig. 8. Thermal conductivity of the paraffin and Ag/PW according to the mass-loading contents.

Fig. 8 shows the effect of the Ag NP size on the thermal conductivity of the Ag/PW. The thermal conductivity increased to 0.270-0.321, 0.273-0.305, and 0.280-0.291 W/m·K for the 9-, 65-, and 300-nm Ag NPs, respectively (0.5, 1.0, 1.5, and 2.0 wt% for each Ag NP size) (the thermal conductivity of paraffin is 0.268 W/m·K). The percolation threshold was between 0.5 and 1.0 wt% in only the 9-nm Ag/PW. The addition of the Ag NPs enhanced the thermal conductivity of the Ag/PW, regardless of the Ag NP size. However, the degree and trend of the thermal conductivity enhancement were different based on the Ag NP size, as shown in Fig. 9. Moreover, at the lowest percentage of 0.5 wt% Ag NPs, the thermal conductivity was the highest and lowest with the 300-nm and

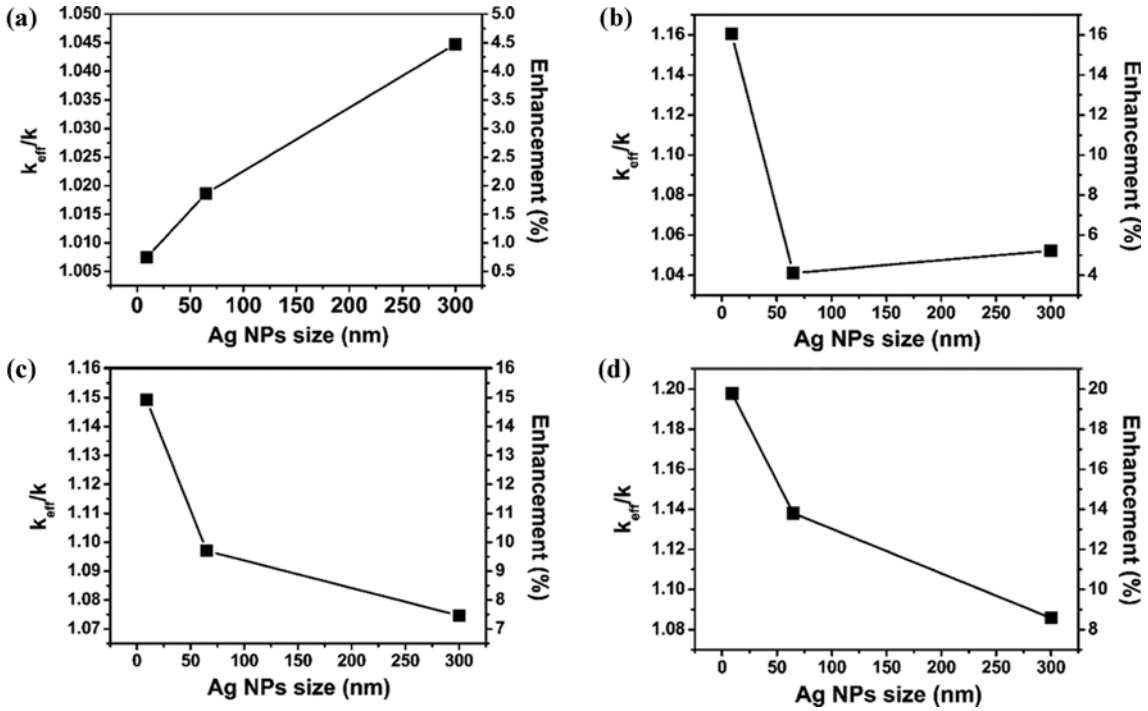

Fig. 9. Enhancement percentage of the thermal conductivity with varying Ag NP loading contents of (a) 0.5, (b) 1.0, (c) 1.5 and (d) 2.0 wt%. Here, k represents the thermal conductivity of pure paraffin, whereas k_{eff} is the thermal conductivity of Ag/PW.

9-nm Ag NPs, whereas the measured highest and lowest thermal conductivities were reversed at the highest loading percentage of 2.0 wt% Ag NPs. Moreover, at 9-nm Ag/PW, the thermal conductivity increased dramatically at 1.0 wt%. This trend was attributed to two factors. First, the interfacial resistance may be a more important factor at the low loading percentage (0.5 wt%).

Burger et al. reported that the size and shape (i.e., aspect ratio) of the filler was an important factor in enhancing the thermal conductivity of the composite [34]. Park et al. and Chritoc et al. reported that long fillers enhanced the thermal conductivity more than that of the short fillers in the composites [35,36]. Mortazvi et al. showed that higher enhancements were achieved with plate fillers than that with spherical fillers [37]. These results indicate that larger fillers are more effective than small fillers at enhancing the TCC thermal conductivity [38-40]. As previously mentioned, the small fillers have a large surface area, leading to an increased thermal resistance and phonon scattering, which is less efficient at enhancing the thermal conductivity. Aggregated particles were not observed on the surface, indicating that the Ag NPs were well-dispersed at 0.5 wt%, as shown in the FE-SEM images (Fig. 4). Thus, the enhancement of the thermal conductivity of the 9-nm mixture was the lowest. The second factor is the formation of Ag NP clusters by the aggregations, depending on the Ag NP size. The number of clusters increased with an increase in the Ag NP loading content, leading to more clustering and randomly connected thermal networks. The cluster formed by the aggregation of the particles had a narrower surface area than that of the independently dispersed particles, leading to less phonon scattering and thermal resistance. When the Ag NP loading percentages increased from 0.5 to 1.0 wt%, each particle aggregated to form a network, except for the 65- and 300-nm sizes, which caused rapid changes in the thermal conductivity of the 9-nm particles in this region.

There are various models for determining the thermal conductivity of two-phase materials. The Maxwell model and Maxwell-Eucken model [41] were adopted to predict the thermal conductivity of the Ag/PW. This model is mainly used at low fractions of spherical particles in two-phase systems, expressed as

$$k_{eff} = k_p \frac{2k_p + k_{np} - 2b(k_p - k_{np})}{2k_p + k_{np} + b(k_p - k_{np})}, \quad (1)$$

where b is the volume fraction of Ag NPs; k_{eff}, k_p, and k_{np} are the thermal conductivities of the Ag/PW, paraffin, and Ag NPs, respectively. We used the mass fraction of the Ag NPs during the experiment, which could be converted to the corresponding volume fraction using the Nabil method [42].

$$b = \frac{m_{wt}\rho_p}{m_{wt}\rho_p + (1 - m_{wt})\rho_{ap}} \quad (2)$$

The parameter b is the volume fraction of the Ag NPs in the Ag/PW, where m_{wt}, ρ_p, and ρ_{ap} are the mass fractions of the Ag NPs in the Ag/PW and the densities of the pure paraffin and Ag/PW, respectively. As shown in Fig. 10(a), the enhancement of the thermal conductivity obtained from the experiment was larger than that predicted by the Maxwell-Eucken model, which was consistent with Nabil's result. The difference between the experimental and theoretical value was larger when the particle content increased.

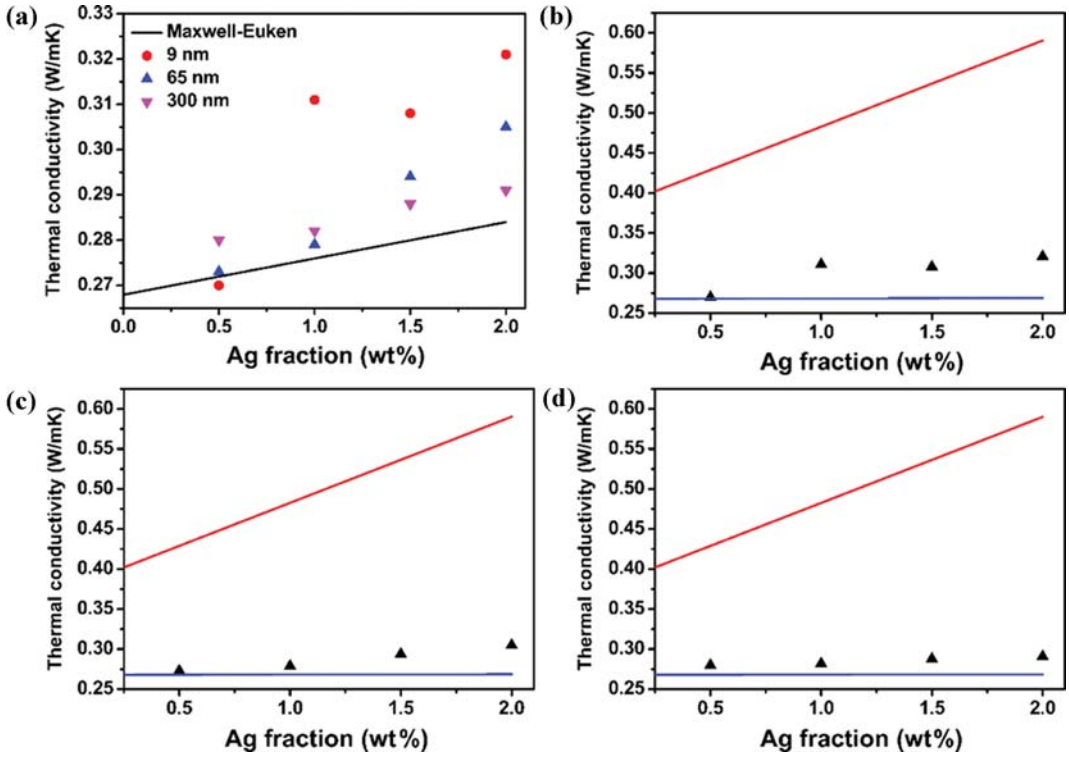

Fig. 10. (a) Relative thermal conductivity of the predictions of the Maxwell-Eucken model: upper (red line) and lower (blue line) H-S bounds of the Ag/PW with varying Ag NP sizes of (b) 9 nm, (c) 65 nm and (d) 300 nm.

These results showed that there were other factors enhancing the thermal conductivity, besides the content of the Ag NPs. The measurement was also compared with the Hashin-Shtrikman model (H-S model) to estimate the lower and upper bounds of the thermal conductivity, as shown below [43].

$$k_p\left[1+\frac{3b(k_{np}+k_p)}{3k_p+(1+b)(k_{np}-k_p)}\right]\le k_{eff}\le k_{np}\left[1+\frac{3b(1-b)(k_{np}+k_p)}{3k_{np}-b(k_{np}-k_p)}\right] \quad (3)$$

The lower H-S limit is for the well-dispersed and isolated particles, where the thermal conductivity closes to a series mode. However, the upper limit corresponds to the particles aggregated and perfectly formed, connecting network structures in the composite. The thermal conductivity closes to the parallel mode [44]. Figs. 10(b)-11(d) show the experimental thermal conductivity with the lower and upper H-S bounds, indicating that, as the Ag NP content increased, the thermal conductivity shifted to the upper limit. Because the experimental result was between the lower and upper bounds of the H-S model, the Ag NPs contained in the Ag/PW were in a distributed cluster state. However, the experimental results are very much closer to the lower bound. Ganesan et al. reports that without chain-forming nanoparticles aggregation can be detrimental to the thermal conductivity enhancement [45]. Chen et al. also shows that thermal conductivity enhancement is achieved through a thermally conductive network which is formed by continuous connection of metal particle clusters [46]. These results indicate that the thermal conductivity enhancement is reliant on the conformation of nanoparticle aggregates. In our result, Fig. 4 confirms that the Ag NPs are aggregated, and the number of clusters increase with the amount of Ag NPs content, but the connectivity of the clusters is very poor. Thus, the Ag/PW shows a much lower thermal conductivity than the maximum value (upper bound), which is actually close to the lower bound predicted by the H-S model.

CONCLUSIONS

Three different sizes of Ag NPs (9, 65, and 300 nm) were mixed with paraffin to create a thermally conductive composite, and the effect of the size on the thermal properties of the composite was investigated. The Ag NPs were well dispersed in the paraffin by ultra-sonication in the paraffin regardless of the particle size. However, with an increase of the Ag NP content, each particle could aggregate, and the number of clusters varied depending on the particle size. The thermal properties of the Ag/PW, such as the thermal stability, latent heat capacity, and thermal conductivity, were also affected by the Ag NP size. The thermal stability and heat storage performance could be explained by the interaction between the paraffin and Ag NPs. Because the 9-nm Ag NPs had a larger surface area than those of the 65- and 300-nm Ag NPs under the same condition, the interaction with the surrounding paraffin was improved, thus improving the thermal stability and crystallization of the Ag/PW. The thermal conductivity of composite was enhanced by addition of Ag NPs, regardless of particle size. However, the degree and trend of the thermal conductivity enhancement are different from the Ag NPs size. The thermal conductivities of each Ag/PW increase as 0.75-19.78% (0.270-0.321 W/m·K), 1.86-13.81% (0.273-0.305 W/m·K), and 4.48-8.58% (0.280-0.291 W/m·K) with 9, 65, and 300 nm sized Ag NPs. In addition, the degree and trend of the thermal conductivity enhancement were different based on the Ag NP size, and the percolation threshold of the Ag/PW on the thermal conductivity was between 0.5 and 1.0 wt% for the 9-nm Ag/PW. Such as difference is qualitatively explained on the basis of the interfacial resistance and aggregation behavior depending on the Ag NPs size. The 9-nm Ag NPs have a higher surface energy than those of the other sizes, which is more advantageous for cluster formation by aggregation owing to the trend of the thermal conductivity improvement. The experimental results were consistent with the theoretical predictions. The thermal conductivity of the Ag/PW was higher than that predicted by the Maxwell-Eucken theorem and was located between the upper and lower bounds of the H-S model. Our study provides progressive insights for developing a thermal energy storage method with highly efficient thermal properties.

AUTHOR CONTRIBUTIONS

All authors have given approval to the final version of the manuscript.

ACKNOWLEDGEMENTS

This work was supported by the Korea Institute of Energy Technology Evaluation and Planning (KETEP) grant funded by the Korea government (No. 20162010104620, The Heat Delivery Technology by Thermal Energy Equipment based Phase Change or Chemical Heat Storage).

REFERENCES

1. V. Etacheri, R. Marom, R. Elazari, G. Salitra and D. Aurbach, *Energy Environ. Sci.*, **4**, 3243 (2011).
2. B. Scrosati and J. Garche, *J. Power Sources*, **195**, 2419 (2010).
3. A. Suwono and G. A. Mansoori, *Energ. Source.*, **16**, 117 (1994).
4. H. Yin, X. Gao, J. Ding and Z. Zhang, *Energy Convers. Manag.*, **49**, 1740 (2008).
5. S. R. White, P. T. Mather and M. J. Smith, *Polym. Eng. Sci.*, **42**, 51 (2002).
6. S. Nikkeshi, M. Kudo and T. Masuko, *J. Appl. Polym. Sci.*, **69**, 2593 (1998).
7. R. Zhang, K.-s. Moon, W. Lin and C. P. Wong, *J. Mater. Chem.*, **20**, 2018 (2010).
8. S. Wu, H. Wang, S. Xiao and D. Zhu, *Procedia Eng.*, **31**, 240 (2012).
9. J. Tigner, M. M. Sedeh, T. Sharpe, A. Bufford and T. Floyd-Smith, *Appl. Therm. Eng.*, **60**, 88 (2013).
10. S. Kim and L. T. Drzal, *Sol. Energy Mater. Sol. Cells*, **93**, 136 (2009).
11. A. Zabalegui, D. Lokapur and H. Lee, Int. *J. Heat Mass Transf.*, **78**, 1145 (2014).
12. F. Yavari, H. R. Fard, K. Pashayi, M. A. Rafiee, A. Zamiri, Z. Yu, R. Ozisik, T. Borca-Tasciuc and N. Koratkar, *J. Phys. Chem. C*, **115**, 8753 (2011).
13. F.-Y. Yuan, H.-B. Zhang, X. Li, X.-Z. Li and Z.-Z. Yu, *Compos. Part A Appl. Sci. Manuf.*, **53**, 137 (2013).
14. S. Kemaloglu, G. Ozkoc and A. Aytac, *Polym. Compos.*, **31**, 1398

(2010).
15. J. Guo, P. Saha, J. Liang, M. Saha and B. P. Grady, *J. Therm. Anal. Calorim.*, **113**, 467 (2013).
16. J.-W. Bae, W. Kim, S.-H. Cho and S.-H. Lee, *J. Mater. Sci.*, **35**, 5907 (2000).
17. N. Tsutsumi, N. Takeuchi and T. Kiyotsukuri, *J. Polym. Sci. Part B Polym. Phys.*, **29**, 1085 (1991).
18. H. Wu and L. T. Drzal, *Polym. Compos.*, **34**, 2148 (2013).
19. W. Zhou, S. Qi, C. Tu, H. Zhao, C. Wang and J. Kou, *J. Appl. Polym. Sci.*, **104**, 1312 (2007).
20. K. Pashayi, H. R. Fard, F. Lai, S. Iruvanti, J. Plawsky and T. Borca-Tasciuc, *J. Appl. Phys.*, **111**, 104310 (2012).
21. T. Shizuma, K. Miyasaka and K. Ishikawa, *J. Macromol. Sci. B.*, **22**, 601 (1983).
22. S.-Y. Fu, X.-Q. Feng, B. Lauke and Y.-W. Mai, *Compos. B Eng.*, **39**, 933 (2008).
23. Z. Zhang and X. Fang, *Energy Convers. Manag.*, **47**, 303 (2006).
24. A. Sarı and A. Karaipekli, *Appl. Therm. Eng.*, **27**, 127 (2007).
25. H. Hiramatsu and F. E. Osterloh, *Chem. Mater.*, **16**, 2509 (2004).
26. U. Holzwarth and N. Gibson, *Nat. Nanotechnol.*, **6**, 534 (2011).
27. M. Chen, Y.-G. Feng, X. Wang, T.-C. Li, J.-Y. Zhang and D.-J. Qian, *Langmuir*, **23**, 5296 (2007).
28. B. A. Korgel, S. Fullam, S. Connolly and D. Fitzmaurice, *J. Phys. Chem. B*, **102**, 8379 (1998).
29. Chandni, N. Andhariya, O. P. Pandey and B. Chudasama, *RSC Adv.*, **3**, 1127 (2013).
30. J. Xiang and L. T. Drzal, *Sol. Energy Mater. Sol. Cells*, **95**, 1811 (2011).
31. S. C. Lin and H. H. Al-Kayiem, *Sol. Energy*, **132**, 267 (2016).
32. B. Li, T. Liu, L. Hu, Y. Wang and L. Gao, *ACS Sustain. Chem. Eng.*, **1**, 374 (2013).
33. Q. Tang, J. Sun, S. Yu and G. Wang, *RSC Adv.*, **4**, 36584 (2014).
34. N. Burger, A. Laachachi, M. Ferriol, M. Lutz, V. Toniazzo and D. Ruch, *Prog. Polym. Sci.*, **61**, 1 (2016).
35. J. G. Park, Q. Cheng, J. Lu, J. Bao, S. Li, Y. Tian, Z. Liang, C. Zhang and B. Wang, *Carbon*, **50**, 2083 (2012).
36. M. Chirtoc, N. Horny, I. Tavman, A. Turgut, I. Kökey and M. Omastová, *Int. J. Therm. Sci.*, **62**, 50 (2012).
37. B. L. Zhu, J. Wang, H. Zheng, J. Ma, J. Wu and R. Wu, *Compos. B Eng.*, **69**, 496 (2015).
38. M. Chirtoc, N. Horny, J.-F. Henry, A. Turgut, I. Kökey, I. Tavman and M. Omastová, *Int. J. Thermophys.*, **33**, 2110 (2012).
39. D. Yu and Q. An, *Polym. Plast. Technol. Eng.*, **48**, 1230 (2009).
40. H. S. Kim, J.-u. Jang, J. Yu and S. Y. Kim, *Compos. B Eng.*, **79**, 505 (2015).
41. J. P. Stora, *Nucl. Technol.*, **17**, 225 (1973).
42. M. Nabil and J. M. Khodadadi, *Int. J. Heat Mass Transf.*, **67**, 301 (2013).
43. Z. Hashin and S. Shtrikman, *J. Appl. Phys.*, **33**, 3125 (1962).
44. P. Keblinski, R. Prasher and J. Eapen, *J. Nanopart. Res.*, **10**, 1089 (2008).
47. V. Ganesan, C. Louis and S. P. Damodaran, *J. Phys. Chem. C*, **122**, 6918 (2018).
46. Y. Chen, W. Luo, J. Wang and J. Huang, *J. Phys. Chem. C*, **121**, 12603 (2017).